



Cite this: DOI: 10.1039/d1ta05379e

Side chain engineering control of mixed conduction in oligoethylene glycol-substituted polythiophenes†

Jonathan W. Onorato,^{†a} Zhongyang Wang,^{‡b} Yangyang Sun,^{‡c} Christian Nowak,^{‡c} Lucas Q. Flagg,^{‡d} Ruipeng Li,^e Ban Xuan Dong,^b Lee J. Richter,^{‡d} Fernando A. Escobedo,^{‡c} Paul F. Nealey,^b Shrayesh N. Patel^{‡b} and Christine K. Luscombe^{‡*afg}

A major limitation for polymeric mixed ionic/electronic conductors (MIECs) is the trade-off between ionic and electronic conductivity; changes made that improve one typically hinder the other. In order to address this fundamental problem, this work provides insight into ways that we could improve one type of conduction without hindering the other. We investigated a common oligoethylene glycol side chain polymer by adjusting the oxygen atom content and position, providing structural insights for materials that better balanced the two conduction pathways. The investigated polymer series showed the prototypical conflict between ionic and electronic conduction for oxygen atom content, with increasing oxygen atom content increasing ionic conductivity, but decreasing electronic conductivity; however, by increasing the oxygen atom distance from the polymer backbone, both ionic and electronic conductivity could be improved. Following these rules, we show that poly(3-(methoxyethoxybutyl)thiophene), when blended with lithium bistrifluoromethanesulfonimide (LiTFSI), matches the ionic conductivity of a comparable MIEC [poly(3-(methoxyethoxyethoxymethyl)thiophene)], while simultaneously showing higher electronic conductivity, highlighting the potential of this design strategy. We also provide strategies for tuning the MIEC performance to fit a desired application, depending on if electronic, ionic, or balanced conduction is most important. These results have implications beyond just polythiophene-based MIECs, as these strategies for balancing backbone crystallization and coordinating group interconnectivity apply for all semicrystalline conjugated polymers.

Received 25th June 2021
Accepted 29th August 2021

DOI: 10.1039/d1ta05379e

rsc.li/materials-a

1. Introduction

Polymer-based mixed ionic/electronic conductors (MIECs) are receiving increased attention, in part due to their utility across a wide-range of applications. MIECs show valuable properties, including volumetric capacitance changes, transduction of

ionic and electronic signals, and biocompatibility.^{1–5} These properties result in a number of useful features, enabling their use in applications such as batteries and ultracapacitors, (bio) sensors, actuators, and organic electrochemical transistors (OECTs).^{6–8} Homopolymer MIECs originally showed limited ionic mobility due to their highly hydrophobic backbones.^{9,10} There has been a significant improvement in their ionic conductivity by introducing polar groups into the solubilizing side chains; the most popular chemistry for the polar side chains is oligoethylene glycol (oEG).^{11–13} This strategy of introducing oEG has driven significant improvements in MIEC performance in a number of conjugated polymer backbones.^{1,14–16}

Side chains are known to have a profound influence on the morphology, crystallinity, charge carrier concentration, charge thermal stability and ion/water uptake properties of conjugated polymers. When the alkyl side chain of poly[2,7-fluorene-*alt*-5,5-(4,7-di-2-thienyl-2,1,3-benzothiadiazole)] was replaced by oEG side chain, the energy barrier of rotating O–CH₂ in oEG side chain was smaller than that of rotating CH₂–CH₂. Compared to the conjugated polymer with alkyl side chain, the more flexible

^aDepartment of Materials Science and Engineering, University of Washington, Seattle, WA 98195, USA. E-mail: luscombe@uw.edu^bPritzker School of Molecular Engineering, University of Chicago, Chicago, IL, USA^cSchool of Chemical and Biomolecular Engineering, Cornell University, Ithaca, NY, USA^dMaterials Science and Engineering Division, National Institute of Standards and Technology, Gaithersburg, Maryland 20899, USA^eNational Synchrotron Light Source II, Brookhaven National Laboratory, Upton, New York, 11973, USA^fMolecular Engineering and Sciences Institute, University of Washington, Seattle, WA 98195, USA^gDepartment of Chemistry, University of Washington, Seattle, WA 98195, USA

† Electronic supplementary information (ESI) available. See DOI: 10.1039/d1ta05379e

‡ These two authors contributed equally to the work.

oEG side chain of conjugated polymer resulted in a tighter π - π stacking, higher crystallinity, and higher charge carrier mobility.^{17,18} For MIECs, the side chains have a two-fold effect as side chains not only influence morphology and thus electronic conductivity, but also because the side chains contain ion-solvating groups that are responsible for ionic conduction. An example of this comes from a naphthalenediimide polymer, where swapping some of the alkyl side chains for oEGs results in a change in morphology and a concomitant three order of magnitude drop in mobility, but also the introduction of ionic conductivity.¹⁶ The manner of attachment of the oEG chains also has a dramatic impact, where increasing the distance between the first oxygen atom in the polymer side chain and the polymer backbone improves both ionic and electronic conductivity, due to increased oxygen atom range of motion and less steric hinderance of the polymer π -stacking behavior.¹⁵ A similar study in polythiophenes shows that by changing the linking strategy (without spacer, with methyl, and ethyl spacer) between the first oxygen atom in the oEG chain and the thiophene backbone, the crystallinity, water uptake and ion uptake change dramatically, which directly affects volumetric capacitance (C^*), transconductance (g_m), and figure of merit ($\mu_{\text{OECT}}C^*$) in fabricated OECTs.¹⁹

It is clear that there is wide variation in the performance of MIEC systems based on the manner of attachment of the oEG side chains, but it is currently not understood how modifying the oEG side chain itself influences the resultant ionic and electronic conductivity.²⁰ A significant consideration is to understand how the side chain's oxygen content and position influences the resulting polymer morphology, electronic conductivity, and ionic conductivity. Herein we investigate a series of polymers with reduced oxygen content relative to the diethylene glycol chain of the MIEC, poly(3-(methoxyethoxyethoxymethyl)thiophene) [P3MEEMT].^{15,19} We first explored 6 permutations of this oEG-substituted polythiophene with a 9-atom side chain using molecular dynamics (MD). The structures of these polymers are shown in Fig. 1.

These simulations illustrated the importance of the increasing solvation site connectivity, showing that reducing the side chain oxygen content while maintaining a high oxygen atom range of motion leads to a high simulated ionic conductivity. Based on those results, we synthesized a subset of those polymers and characterized their solid-state structure, electronic conductivity, and ionic conductivity across a range of lithium bistrifluoromethanesulfonimide (LiTFSI)

concentrations. Ultraviolet-visible (UV-vis) and grazing incidence wide-angle X-ray scattering (GIWAXS) data show that by increasing the distance between coordinating groups and the polymer backbone, greater degrees of organization and crystallinity are achieved, even with high concentrations of LiTFSI. Electrochemical impedance spectroscopy (EIS) highlights that these modified structures and the improved molecular ordering results in improved electronic conductivity as compared to P3MEEMT and other polymers with coordinating groups near the polymer backbone. Ionic conductivity also tends to increase with this distance, though oxygen atom content in the side chain also plays a contributing role. Too much oxygen (P3MEEMT) coordinates Li^+ too strongly, inhibiting ion motion, but too little oxygen limits LiTFSI solubility and reduces solvation site connectivity, resulting in reduced ionic conductivity. The best balance is observed in poly(3-(methoxyethoxybutyl)thiophene) [P3APPT], which, with its two oxygen atoms far from the polymer backbone, shows reasonably strong electronic and ionic conductivity. By studying this range of polymers across LiTFSI doping concentrations, we are able to elucidate how variations in the side chain architecture influence the evolution of morphology with increasing levels of LiTFSI doping, highlighting the importance of the architecture of oEG side chains in determining the blended material's morphology and resultant ionic and electronic conductivity.

2. Methods

2.1 Material synthesis

The detailed monomer and polymer synthesis and characterization are described in the ESI Section S.1.†

2.2 Thin film sample preparation

Polythiophene derivatives (P3PAAT, P3AAPT, P3APPT, and P3PPAT) were dissolved overnight in chlorobenzene (CB) at a concentration of 10 mg mL^{-1} inside an argon-filled glove box. LiTFSI was similarly dissolved overnight at 10 mg mL^{-1} in acetonitrile (ACN) in an argon glovebox. Polymer:LiTFSI blends were prepared at a range of concentrations normalized against the number of ethylene oxide units (EO) in each polymer side chains, targeting molar ratios of $r = [\text{Li}^+]/[\text{EO}] = 0$ (neat polymer), 0.01, 0.05, 0.10, 0.15. For P3AAPT and P3PAAT, this results in a CB/ACN ratio of 4 : 1000, 37 : 1000, 74 : 1000, and 111 : 1000, and for P3APPT and P3PPAT of 14.8 : 1000, 74 : 1000, 158 : 1000, and 222 : 1000. These blends were prepared by filtering polymer solutions through a syringe filter, and then adding LiTFSI/ACN solution to achieve the desired ratio. Following addition of LiTFSI/ACN, the blended solutions were allowed to stir for several hours prior to use to ensure equilibrium mixing. All substrates used for preparing thin film samples were rinsed with acetone and isopropanol several times followed by ozone plasma treatment for 10 min. Thin film samples were prepared by spin casting solutions on substrates at 2000 rpm ($60 \text{ rpm} = 2\pi \text{ rad s}^{-1}$) for 2 min. Film thickness of all samples ranged from 50 nm to 70 nm, as confirmed by spectroscopic ellipsometry measurements.

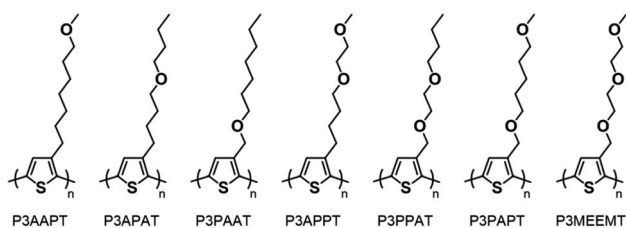


Fig. 1 Full list of possible oligoethylene glycol permutations with a 9 atom-length side chains, as investigated using molecular dynamics.

2.3 ^1H nuclear magnetic resonance (NMR)

NMR spectra for small molecules was taken using a 300 MHz Bruker AV-300 spectrometer, and spectra for polymers was taken using a 500 MHz Bruker AV-500 spectrometer. All spectra were taken in CDCl_3 at room temperature.

2.4 Size exclusion chromatography (SEC)

SEC was performed using a Malvern Viscotek TDA 305 with an attached UV detector using polystyrene molecular weight references. THF at 40 °C and a flow rate of 1 mL min⁻¹ was used as an eluent.

2.5 Ultraviolet-visible (UV-vis) spectroscopy

The UV-vis measurements were performed using a Shimadzu UV-3600 Plus dual beam spectrophotometer at the Soft Matter Characterization Facility (SMCF) at the University of Chicago.

2.6 Atomic force microscopy (AFM)

The surface topographies of thin film samples were characterized by a Cypher ES AFM (Asylum Research Oxford) with FS-15000AuD cantilever at room temperature. The images were acquired using tapping mode and analyzed by using Gwyddion software.²¹

2.7 Thermogravimetric analysis (TGA)

TGA was performed using a TA Instruments Q50 with a heating rate of 10 °C min⁻¹ under a nitrogen environment.

2.8 Differential scanning calorimetry (DSC)

DSC traces were taken on a Mettler Toledo DSC 3+. Blend samples were prepared by preparing a mixed solution of LiTFSI and polymer at the appropriate ratio, r , and then were drop cast into the sample pan at room temperature. Samples were taken through a heat/cool/heat cycle from -90 °C to temperature maximums as dictated by their thermal degradation characteristics (175 °C or 225 °C). Samples were heated and cooled at a 10 °C min⁻¹ rate and were kept under nitrogen flow during the experiment.

2.9 Grazing-incidence wide-angle X-ray scattering (GIWAXS)

Films of each polymer were prepared as described above (Section 2.2) with varying LiTFSI concentration on 1 cm² silicon substrates. The data was collected at Brookhaven National Lab, National Synchrotron Light Source II (NSLS-II), 11-BM Complex Materials Scattering beamline using a 13.5 keV incident X-ray, a detector distance of 258 mm and a 0.14° angle of incidence with respect to the substrate. The detector calibration was performed relative to a silver behenate crystal. GIWAXS data was processed using the Nika software package for Wavemetrics

Igor Pro.^{22,23} Out of plane linecuts are sector averages 10° wide centered around 90°. In plane line cuts are horizontal lines 5 pixels wide centered 9 pixels above the horizon.

2.10 Electrochemical impedance spectroscopy (EIS) and DC measurements

Conductivity measurements were performed on top of interdigitated electrode arrays (IDEs) using a Gamry 600+ potentiostat inside an argon-filled glovebox. Samples were quickly transferred in air between the film-processing glovebox and the testing glovebox. The fabrication details of the IDEs can be found in our previous report.²⁴ The electrical contact was made by using two customized probes with the help of manipulators (Semiprobe Inc.) The EIS was conducted with an applied 60 mV voltage from 1 MHz to 0.1 Hz at different temperatures. The ionic (R_i) and/or electronic resistance (R_e) data were then extracted from the impedance spectrum by fitting an equivalent circuit, with representative examples being shown in Fig. 8. The conductivity σ of the thin film sample was calculated using the following equation:^{15,25}

$$\sigma_{i/e} = \frac{1}{R_{i/e}} \frac{d}{l(N-1)h} \quad (1)$$

where $R_{i/e}$ is ionic/electronic resistance, d is the spacing between adjacent electrode teeth (8 μm), l , the length of the electrode (1000 μm), N is the number of electrodes (160), and h is the thickness of the film.

For DC measurements, potentials between 100 mV to 200 mV with a step of 5 mV s⁻¹ were applied on P3AAPT polymer films to verify the electronic conductivities extracted from the equivalent circuits. The current response was measured using a Gamry 600+ potentiostat and the sample preparation method is the same compared to AC impedance measurements. Conductivity values obtained by DC measurements are derived from eqn (1) and Ohm's law. All conductivity values are from AC impedance unless stated otherwise.

2.11 Computational simulations

Following our previous study,¹⁵ an all-atom model is used to simulate the polymer species shown in Fig. 1. Crystalline and amorphous morphologies are generated for each species. The ion mobility is evaluated by calculating the mean squared displacement (MSD) of simulation trajectories. Umbrella sampling is implemented to investigate the dissociation energy of Li⁺ and TFSI⁻ ion in every targeted polymer. Simulation details are shown in the ESI Section S.6.†

3. Results and discussion

3.1 Molecular dynamics investigations

A common problem in exploring novel polymer chemistries is the time-intensive nature of polymer synthesis. As such, to explore the performance across the full spread of possible side chain oxygen permutations, we first turned to MD to build understanding of the polymer performance and select the best candidates for synthesis. The full range of polymers

† Certain commercial equipment, instruments, or materials are identified in this paper in order to specify the experimental procedure adequately. Such identification is not intended to imply recommendation or endorsement by NIST, nor is it intended to imply that the materials or equipment identified are necessarily the best available for the purpose.

investigated are shown in Fig. 1, with P3MEEMT shown for reference. The polymers are named based on the pattern of inclusion of an ethylene oxide polar moiety (P), or a three-carbon alkyl (A) unit, moving outward from the polymer backbone. The previously studied P3MEEMT is shown for reference. In the convention of this paper, P3MEEMT would be P3PPPT (Fig. S21†), but we will use the original nomenclature in this paper.

Two distinct morphologies were targeted for each side chain modified polymer, crystalline and amorphous (see Section S.6.1† for procedures for structure generation). Representative crystalline structures generated are shown in Fig. 3 and will be discussed later in this section. In order to normalize for the differences in oxygen content in the polymer side chain and thus changes in dissolution power for the different chemistries, we calculated an effective dissociation energy for an LiTFSI molecule for each of the polymers in the crystalline and amorphous states. The method is described in greater detail in the ESI (Section S.6.3†), but briefly, a molecule of LiTFSI was randomly placed into the simulated crystalline or amorphous polymer structure and allowed to equilibrate. Then, the Li^+ and TFSI^- ions were separated until the energy equilibrated, and the resultant potential of mean force (PMF), or energy, change between the initial (associated) and final (dissociated) states were measured and reported as an effective dissociation energy (E_d). The measured E_d represents the approximate “difficulty” of dissociating an LiTFSI molecule and can serve as a proxy for the solubility of LiTFSI.^{26,27} The energy profile during the dissociation process for the crystalline polymer structures are shown in Fig. 2A, and the calculated LiTFSI E_d values for the crystalline polymers are summarized in Fig. 2B. The trends in PMF and E_d are largely the same in the amorphous polymers, though the amorphous simulations typically show slightly lower E_d , as reported in Fig. S21.†

Fig. 2A highlights that there are 4 distinct groupings of PMF profiles, highlighted in different colors. We can see that these

data generally show a correlation between the number of oxygen atoms per side chain and the observed E_d or PMF, with increasing oxygen content leading to a lower E_d and PMF. Two samples are outliers in this trend: P3AAPPT and P3APPT, having markedly lower E_d than other one and two oxygen atom counterparts, respectively. This lower E_d implies that something about their structure is enabling these two polymers to outperform simple oxygen concentration considerations for E_d .

To understand this variation in observed PMF and E_d , profiles of the simulated structures were generated. The regular arrangement of the polymer backbones, and the polar–nonpolar interactions between oEG and alkyl domains in the side chains results in the formation of a nanoscale phase separation between polar and nonpolar domains. The resulting structures are shown in Fig. 3 (complete set in Fig. S23†). In these crystalline structures, the oxygen atom-containing domains are highlighted in red. From these images it can be observed that for both P3AAPPT and P3APPT, a cooperative effect between adjacent polymer backbones results in the formation of an extended solvation domain, giving the P3APPT an effective 4-oxygen atom wide domain, and P3AAPPT a 2-oxygen atom wide domain. This explains why P3AAPPT performs comparably to the two oxygen atom samples rather than the 1 oxygen atom samples, and why P3APPT outperforms other 2 oxygen atom samples in terms of E_d .

Ionic conductivity for all polymer samples was calculated using MD. A brief description is given here, and a more detailed one is presented in the ESI (Section S.6.2†). After generating each structure and calculating E_d , the ionic conductivity of each polymer system for Li^+ in either the crystalline or amorphous structures were calculated as follows. Freely dissociated Li^+ ions were placed into the polymer structure one at a time, and their position tracked over time upon the application of an electric field. The fraction of mobile ions was multiplied by this drift and normalized by E_d to account for differences in ion solubility. Eqn (2) summarizes this calculation, where σ is the

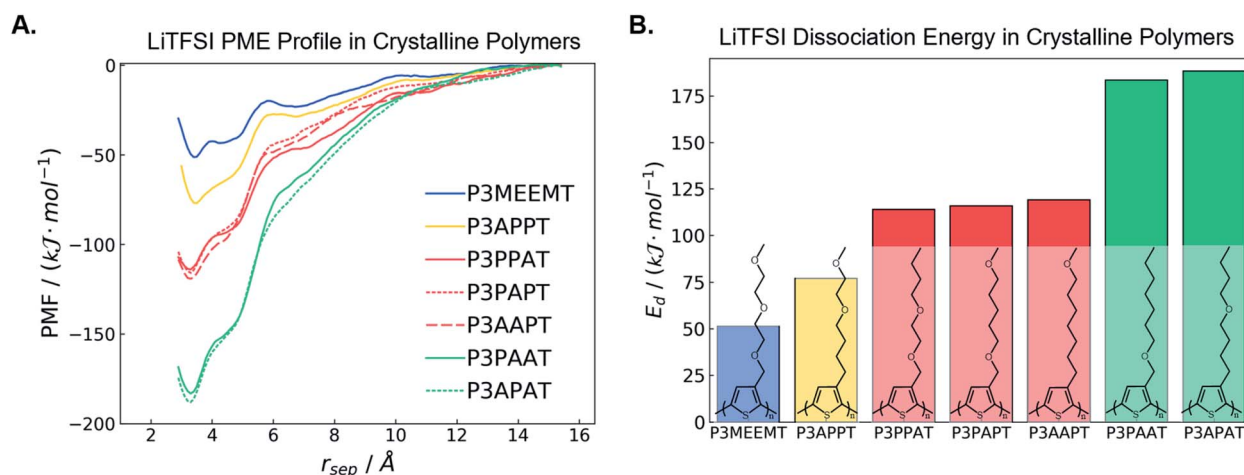


Fig. 2 (A) Potential of mean force associated with LiTFSI across different cation–anion separation distances in the different crystalline polymer environments. (B) Extracted simulated dissociation energies for LiTFSI in different crystalline polymer environments. Matching colors indicate qualitatively similar groupings of PMF profiles. Chemical structures of P3MEEMT derivatives are inserted into the bar chart for readers' convenience.

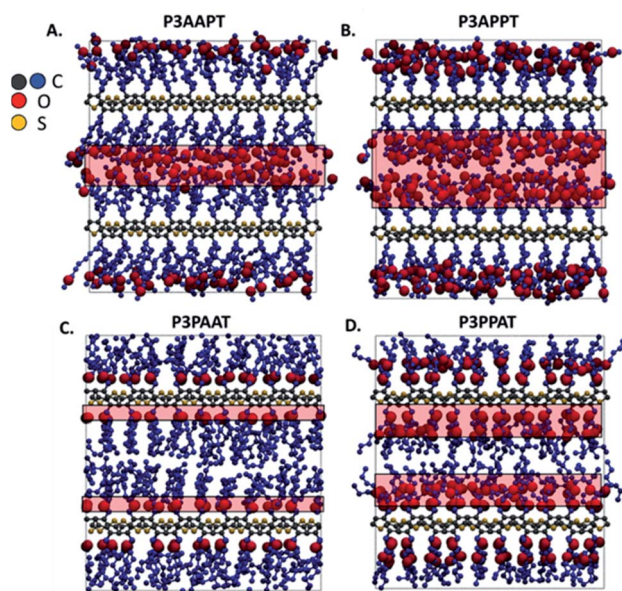


Fig. 3 Solubilizing domains of parallel polymer backbones within a crystallite for (A) P3AAPT, (B) P3APPT, (C) P3PAAT, (D) P3PPAT. Atoms are identified by color (see inset), with blue atoms representing side chain carbons, and black backbone carbons.

normalized ionic conductivity, q is the ion valence (1 in this case), v is the drift velocity, n is the number density of dissociated ions, and E_d is the dissociation energy:

$$\sigma = \frac{qvn}{E_d} \quad (2)$$

Fig. 4 shows the calculated ionic conductivity normalized against the value for P3MEEMT. From Fig. 4, it is clear that kinetic considerations ($v \times n$) can dominate the population (E_d) trends. Focusing on the crystalline samples (Fig. 4a), it is seen that the three highest performing polymer samples have a terminal coordinating atom along the side chain. This suggests that oxygen atoms at the end of the side chain attract the ion to the end of the chain and facilitates rapid transport. The low performers, P3PAAT,

P3PPAT, and P3APAT all have high oxygen atom density towards the polymer backbone, limiting the hopping behavior for a coordinated Li^+ ion. Overall, there is a net increase in ionic conductivity when the coordinating atoms are further away from the polymer backbone. This effect is also conflated with the number of coordinating atoms in the side chain, where increasing the number of oxygen atoms results in a reduction in ionic conductivity. When looking at the amorphous simulation data, while the drift velocity is still dependent on having oxygen atoms at the end of the polymer chain, it is more important that there are a significant number of oxygen atoms in the side chain. As such, all polymers perform less well than the amorphous P3MEEMT. The significant reduction in relative performance for the amorphous P3AAPT is likely due to a reduction in solvation site connectivity.

The associated E_d values for the polymers largely decrease with increasing oxygen content; the outliers form extended solvation domains across multiple polymer backbones. When considering the overall conductivities, the population-based trend (E_d) can be dominated instead by drift kinetics (*i.e.* v is more indicative of ionic conductivity than E_d). The crystalline conductivity depends on solvation site connectivity, with oxygen atoms at the end of the side chain resulting in the best conductivities; the amorphous conductivities also follow this trend, though are also significantly dependent upon oxygen atom count in the side chain, with more oxygen atoms leading to improved ionic conductivity. While crystalline conductivity is enlightening and potentially plays a supporting role in ionic conductivity for these polymers, it is expected that the amorphous domains of the conjugated polymers will be predominately responsible for ionic conduction. Based on the observed performances and trends, and our interest in understanding the effect of the full range of possible oxygen atom content and positioning, the P3AAPT, P3APPT, P3PAAT, and P3PPAT systems were selected for experimental characterization.

3.2 Polymer morphology and LiTFSI doping

P3AAPT, P3APPT, P3PAAT, and P3PPAT were synthesized following a Kumada Catalyst Transfer Polymerization (KCTP)

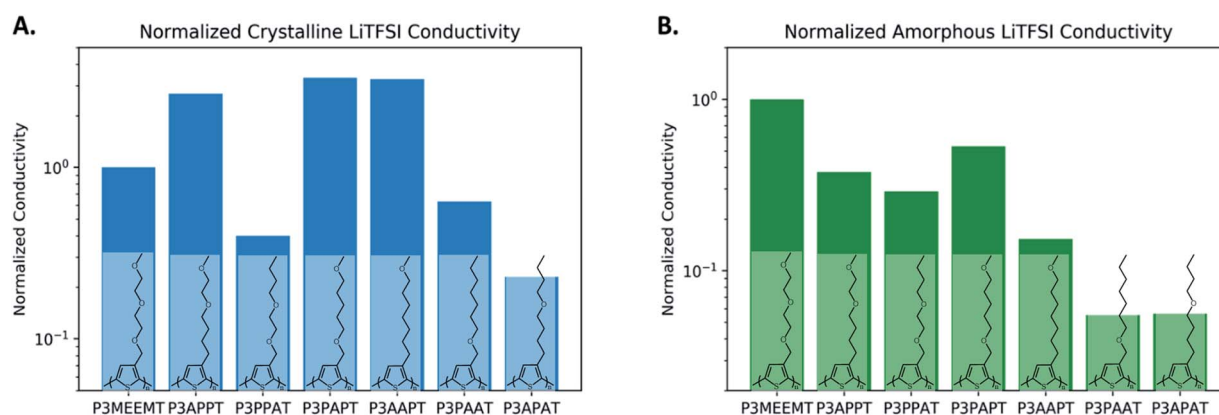


Fig. 4 Calculated ionic conductivity values for (A) crystalline and (B) amorphous polymer samples, normalized with the respective polymer dissociation energies, and further normalized against the P3MEEMT performance ($\text{P3MEEMT} = 1$). Chemical structures of P3MEEMT derivatives are inserted into the bar chart for readers' convenience.

from their respective dibrominated monomers. The specific details of the monomer and polymer syntheses are described in the ESI (Section S.1†), with reaction schemes shown from Fig. S1–S6† and the resultant polymer number average molecular masses (M_n) shown in Table 1. The M_n are similar, thus enabling cross-comparison between different polymer samples.

Once prepared, polymer films in their neat and LiTFSI-blended states were characterized using UV-vis spectroscopy to clarify differences in their solid-state packing behavior. A major focus was on understanding the influence of both oxygen content and position on the structure and its evolution with increasing LiTFSI content. To provide a controlled comparison between samples, the LiTFSI content was normalized for each polymer based upon the number of ethylene oxide repeat units present in the side chain, following eqn (3):

$$r = \frac{[\text{LiTFSI}]}{[\text{No. of ethylene oxide repeat units}]} \quad (3)$$

The observed UV-vis spectra are shown in Fig. 5. The unannealed films were spin-cast from chlorobenzene, a high boiling solvent that gives a long time for self-organization and crystallization.^{28,29} P3AAPT and P3APPT in their neat solid states show the appearance of a vibronic progression, a feature which is indicative of increased planarization and self-organization of the polymer backbone.^{30,31} The absorption profile of both polymers matches well with poly(3-hexylthiophene) [P3HT], with nearly identical absorption onsets [P3HT onset = 660 nm, P3AAPT and P3APPT onset = (657 to 664 nm)].³² Neither P3PAAT nor P3PPAT show such a vibronic progression; this variation is likely due to the presence of the oxygen atom adjacent to the thiophene backbone which hinders the chain's ability to planarize. As compared to P3MEEMT the absorption onsets and maxima of P3AAPT and P3APPT are redshifted consistent with increased planarization, whereas the absorption maxima for P3PAAT and P3PPAT are blueshifted.¹⁵ This indicates that it is not simply the oxygen atom proximal to the backbone that leads to a blueshift. We hypothesize that the degree of ordering of the side chain is responsible for the difference in absorption maxima of P3MEEMT ($\lambda_{\text{max}} = 500$ nm) and P3PAAT or P3PPAT [(466 and 473) nm, respectively]. This hypothesis is partially supported by the DSC data. Previously, side chain crystallinity has been observed for P3MEEMT (at 65 °C), but no significant amount was observed in this work for P3PAAT or P3PPAT.¹⁵ Upon addition of LiTFSI there are small changes in the absorption profile for P3AAPT and P3APPT which are best captured in changes in the ratio between A_{0-0} and A_{0-1} , as discussed in the ESI (Section S.3†), and summarized in Table S1.†^{30,31} Overall, it is seen that a proximal oxygen atom results in

reductions in along-backbone ordering, and by pushing the oxygen farther from the backbone we see improved planarization and the appearance of a vibronic progression.

It is well known that increasing along-backbone order results in an improvement in electronic mobility in polythiophene derivatives. Further, ionic conductivity is strongly linked to mobility of ionically conducting groups, implying that lower glass transition temperature (T_g) values and lower crystallinity of side chain domains will improve ionic conductivity. Understanding the evolution of these structural habits of these polymers is critical to understanding their ionic and electronic conductivity performance. As such, the connection between chemical structure and crystallinity was investigated through several thermal characterization methods. The polymers displayed markedly different decomposition temperatures as observed through thermogravimetric analysis (TGA), as shown in Fig. S7.† Again, a split is seen where P3AAPT and P3APPT (>350 °C) show higher decomposition temperatures than P3PAAT (310 °C) and far higher than P3PPAT (170 °C), highlighting the destabilizing effects of a proximal oxygen atom.

To better understand the crystalline behaviors of the neat polymers differential scanning calorimetry (DSC) was used across temperature ranges as dictated by the polymer decomposition temperatures. The overlaid traces of these polymers in their neat and LiTFSI blended states are shown in Fig. S8–S11.† Both side chain and backbone crystallinity are considered, the former for its importance for ionic conductivity, and the latter for electronic charge transport. The measured melting or crystallization temperatures and embodied enthalpies for the different thermal transitions are listed in Table S2.†

Comparing the neat samples, it is clear that both P3AAPT and P3APPT are more crystalline than P3PAAT and P3PPAT, with both showing clear and strong backbone and side chain melting transitions. Both polymers show multiple overlapping backbone melting peaks, indicating chain extended crystals with a dispersity of crystallizable lengths.³³ P3PAAT shows a weak melting transition at an intermediate temperature, a transition we assign to a side chain melting, though no backbone melting. P3PPAT shows a thermal profile with no obvious transitions.

In addition to the neat samples, DSC was performed on the LiTFSI blended polymers to characterize their structural evolution with the introduction of salt. P3AAPT's side chain melting transition shows little change with LiTFSI, even up to $r = 0.15$, indicating that the side chain crystallization habit is minimally affected by the presence of salt. The backbone-crystallization transition changes its crystallization temperatures as higher levels of LiTFSI are introduced. P3APPT, unlike P3AAPT, has a reduction in the relative crystallinity with increasing LiTFSI, eventually seeing full suppression of side chain crystallinity at $r = 0.10$ and 0.15 and significant reduction of the backbone crystallinity at $r = 0.15$. This could imply that the P3AAPT crystallinity is less sensitive to LiTFSI introduction, though it is also possible this difference could be due to the greater molar concentration of LiTFSI in P3APPT at the same r relative to P3AAPT. There is also an initial backbone peak broadening and reduction in peak size, which eventually splits

Table 1 Polymer number average molecular mass (M_n) and dispersity (\bar{D}) for all polymer samples from SEC

	P3AAPT	P3APPT	P3PAAT	P3PPAT
M_n (kg mol ^{−1})	12.4	10.5	9.1	12.4
\bar{D}	1.4	1.5	1.9	1.5

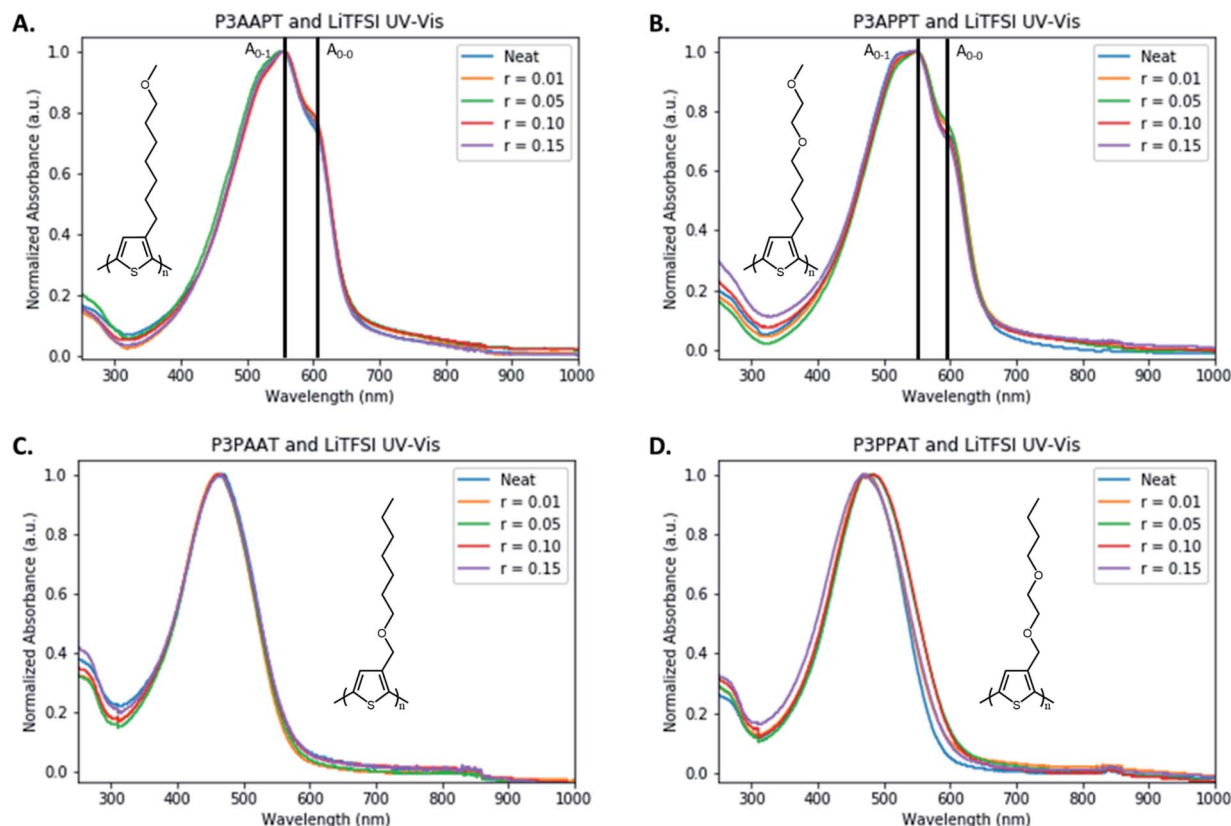


Fig. 5 UV-vis absorption spectra for all polymers with LiTFSI doping. For P3AAPT (A) and P3APPT (B) the 0–0 and 0–1 transitions are marked with vertical lines to aid the eye.

the melting signal into two distinct peaks at high LiTFSI ($r = 0.15$). This new phase is not a pure LiTFSI crystal, as the temperature is incorrect for an LiTFSI transition ($T_m = 234\text{ }^\circ\text{C}$, $T_{\text{solid-solid}} = 152\text{ }^\circ\text{C}$), and may instead be some form of mixed phase.³⁴

Both P3PAAT and P3PPAT have largely featureless DSC profiles, excluding the already-discussed neat P3PAAT. It was not possible to confidently determine T_g values for any of the polymers at any LiTFSI level, a problem commonly seen in polythiophenes.^{35,36} Overall, we see that when oxygen atoms are close to the backbone, backbone crystallization is limited. The lack of a backbone melt, in addition to the relatively high degree of backbone torsion as seen in the UV-vis, suggests that P3PAAT and P3PPAT will have poorer electronic conductivity than either P3AAPT or P3APPT, as typically strong π -stacking and backbone order is needed in polythiophene-based electronic conductors.

This DSC analysis was complemented by GIWAXS, to better understand the nature of the structural evolution of the crystalline regions of the polymer with increasing LiTFSI concentration. A figure of all observed linecuts from the in and out of plane directions are presented for all polymers and LiTFSI concentrations in Fig. S12,[†] and the raw diffractograms are shown in Fig. S13.[†] A summarized comparison of the neat and $r = 0.15$ films of all polymers in the in and out of plane directions are shown in Fig. 6.

The P3AAPT crystal structure seems to be relatively robust and unchanging upon introduction of LiTFSI, retaining higher

ordered side chain reflection peaks, as well as most of the relatively strong diffraction intensity, in both the (100) and (010) directions, an observation that aligns with the DSC data. P3APPT shows a similar degree of robustness in the crystal structure, though to a lesser degree than seen for P3AAPT, again correlating well with the DSC data. The (100) peak maintains a high intensity throughout, but the (200) diminishes at high LiTFSI loading. The (300) peak follows an unusual evolution as it initially fades, but eventually increases significantly at $r = 0.15$. This increase coincides with the appearance of a new peak at $q = 1.4\text{ }\text{\AA}^{-1}$. It is possible that these two changes correspond to the new π -stack melting temperature observed in the DSC data also at $r = 0.15$ and could be indicative of a new crystalline phase. Alternatively, this “(300)” peak could instead be the (001), allowed by the formation of an ordered alloy of P3APPT with LiTFSI, the diffraction peak of which would occur at a similar position as the (300).

P3PAAT's diffractogram shows a reduction in diffraction intensity for all peaks except the (100) with increasing LiTFSI concentration. In the in plane direction we see an initial small (010) peak that is suppressed at $r = 0.15$; the out of plane direction shows little to no (010) diffraction intensity for all levels of LiTFSI. P3PPAT exhibits a variety of small changes in the diffraction pattern with increasing r , the most notable of which is the disappearance of the initially relatively weak (200) peak at $r = 0.10$ and 0.15 . Through this, the (300) peak appears

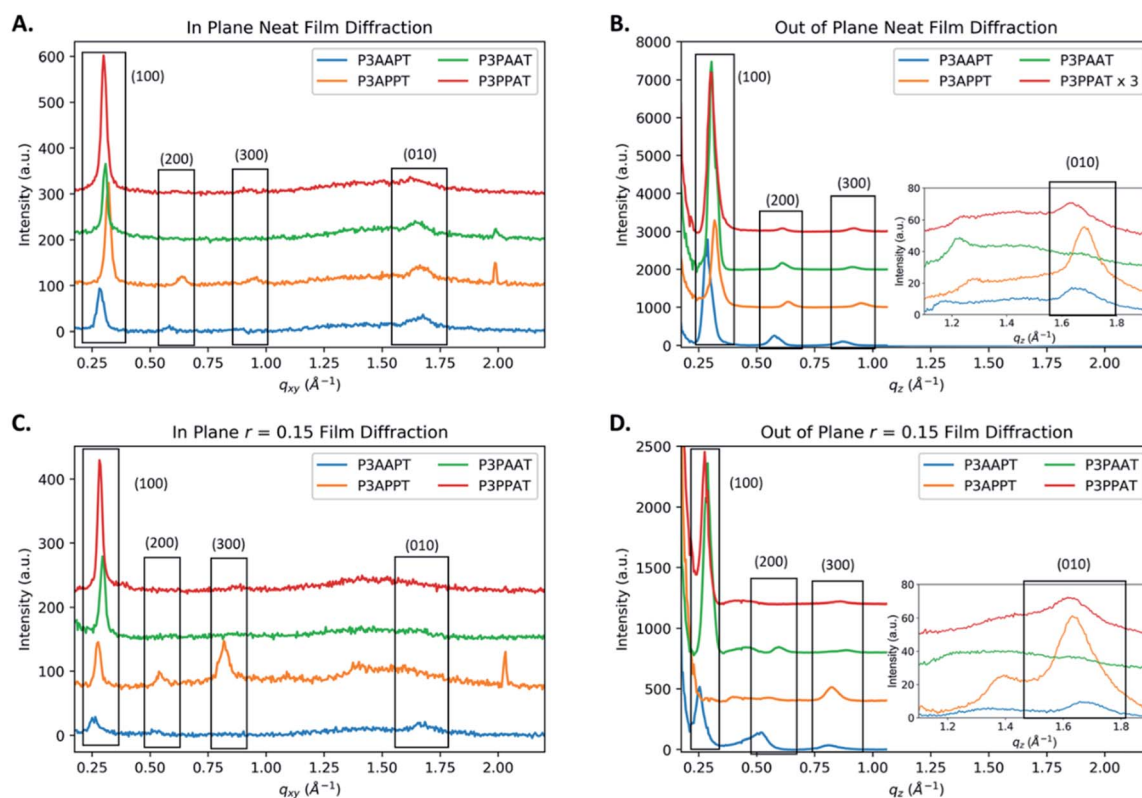


Fig. 6 (A) In plane and (B) out of plane diffraction cuts of neat polymer samples. (C) In plane and (D) out of plane diffraction cuts at $r = 0.15$ for all polymers. Note that traces are offset vertically for visual clarity. Different crystallographic direction peak locations are bounded with boxes and labelled for clarity. To enable visibility of weaker features in P3PPAT, the out of plane, neat diffraction (B) was multiplied by a $3\times$ multiplication factor.

relatively unchanging in intensity. The (010) peak appears to be relatively consistent in the out of plane direction.

All films are predominately edge-on with P3AAPT and P3APPT showing a moderate amount of mixed (face and edge) character, though all but P3PAAT show a discernable fraction of isotropic diffraction. This edge-on behavior is similar to what has been observed in other oEG-substituted thiophenes.^{1,15,19,37} The observed (100) d -spacings are somewhat similar, with P3APPT (19.7 Å) being smaller than the rest, (20.5 to 21.9) Å, indicating a more coiled side chain architecture. All polymers have nearly identical (010) d -spacings, (3.72 to 3.83) Å. The d -spacings for all observed peaks across all samples are shown in Table S2.† Comparing the $r = 0.15$ data as shown in Fig. 6C and D, further emphasizes the side chain driven differences. As salt is taken into the crystal structure, the side chain distance increases to accommodate the additional molecules. Due to the extra swelling of the P3APPT, it is instead the P3PAAT system which shows the smallest $r = 0.15$ (100) d -spacing, at 21.9 Å. Because of the initially small d -spacing of P3APPT, in spite of the P3APPT high swelling percentage P3AAPT remains the largest d -spacing, at 24.9 Å, as compared to P3PPAT (22.8 Å) and P3APPT (22.8 Å). As with the neat films, the (010) d -spacing remains relatively comparable across all polymers (3.74 to 3.86) Å. The molecular orientation also switches for some samples,

with P3PPAT adopting a face-on configuration, and P3AAPT switching to a mixed face on and edge on configuration.

The variations in d -spacing were summarized by their percent change, or swelling, in Fig. 7A for the (100) plane, and Fig. 7B for the (010) plane. The swelling percentages reported herein are derived from taking the (100) and the (010) plane d -spacings in a singular direction (in plane or out of plane across all r) and comparing against the neat d -spacing. The full table of measured peak positions and d -spacing for each crystallographic peak are shown in the ESI, in Table S3,† and the percent swelling is shown in Table S4.† The π -stacking direction shows no significant variation about their equilibrium d -spacing, indicating minimal impact of LiTFSI introduction on the (010) spacing for all polymer side chain architectures, as shown in Fig. 7B. This result aligns well with P3MEEMT data, as well as other polythiophenes blended with lithium salts.^{37–39} These polymers do not demonstrate the typical reduction in the (010) spacing characteristic in highly doped polythiophenes, indicating that there is not a significant amount of electronic doping occurring.⁴⁰ The (100) direction instead shows large changes with LiTFSI. As side chains are expected to be responsible for solvating the dissolved ions, we correlate the increasing side chain distance with an increase in the amount of LiTFSI ions incorporated into the polymer crystal structure. P3APPT experiences the greatest amount of swelling, followed

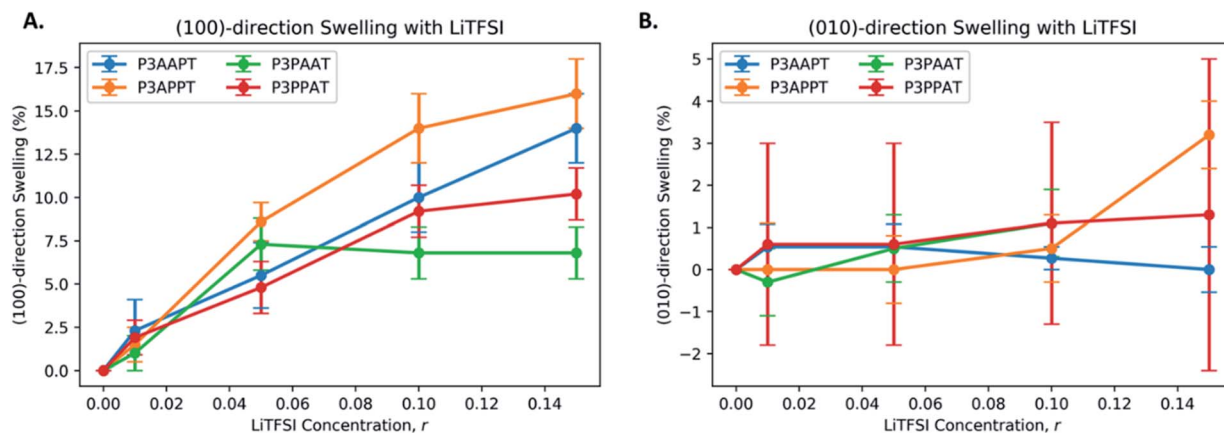


Fig. 7 Swelling of the (A) (100) and (B) (010) directions upon introduction of LiTFSI.

by P3AAPT, then P3PPAT, and finally P3PAAT. Comparing against the swelling profiles for P3MEEMT and P3MEET, also oEG-substituted polythiophenes, P3PAAT shows similar swelling behavior, initially swelling then saturating, though it saturates at a much lower swelling percentage.¹⁵ P3AAPT, P3APPT, and P3PPAT instead show more continuous uptake of LiTFSI, indicating a more balanced solubility between the crystalline and amorphous regions.¹⁵ The lack of continued swelling for P3PAAT above $r = 0.05$ is potentially due to the saturation of the crystallite phase with LiTFSI; it is possible that this saturation occurs in the amorphous regions as well, but due to the lack of a distinct LiTFSI diffraction pattern widespread phase separation is unlikely. It should be noted that for all polymers and LiTFSI concentrations, AFM data indicates minimal change in the surface morphology, even upon appearance of the new melting transitions and diffraction signals (Fig. S14†).

P3AAPT sees a higher (100) swelling percentage than that observed for P3PAAT. This is consistent with the hypothesis that by having the polymer side chains between adjacent crystalline backbones able to organize into an “EO-layer” as shown in Fig. 3, the crystalline domains (and potentially also the amorphous domains) are better able to solubilize Li salts. A larger domain, as seen in P3APPT, further increases that crystalline solubility as evidenced by the larger degree of swelling. This highlights that not only the amount of oxygen atoms or their relative range of motion, but also their degree of interconnectedness, or solvation site connectivity, has a significant impact on solubility in these polymers. Overall, it is clear that there is salt uptake into the crystalline and amorphous regions for all four polymers, with no large-scale phase segregation.

3.3 Electronic and ionic conductivity

To probe the electronic and ionic conductivity of the polymers, samples with a range of LiTFSI concentrations were prepared by spin coating thin films on a set of interdigitated electrodes, then characterized using electrochemical impedance spectroscopy (EIS). An alternating current was applied with varying frequencies, and the impedance data was fit with an equivalent circuit

model to extract ionic and electronic conductivities for each polymer sample. An optical image of the electrodes, and representative Nyquist plots and equivalent circuit models are shown in Fig. 8. EIS shows the dominant conductivity pathways for charge in a polymer sample; if the ionic and electronic conductivity are not relatively balanced, EIS will only be able to detect the dominant pathway. The plots in Fig. 9 show the measurable data points – any data points not shown are absent due to their being too low to measure or being orders of magnitude lower intensity than another conduction mechanism.

When considering electronic conductivity, there are contributions from not only the mobility, but also charge carrier concentration. Usually, intrinsic charge carrier concentrations in conjugated polymers are the result of chemical defects from the synthesis. All four polymers demonstrate some amount of electronic conductivity, though there are significant differences between the different polymer structures and LiTFSI concentrations. All four polymers were synthesized and purified following identical procedures and thus would be expected to have similar intrinsic defects and chemical impurities. As such, we expect that any differences in the electronic conductivity are due to differences in how the polymer structure interacts with oxygen, as well as the introduced LiTFSI. Atmospheric oxygen and ozone have been shown to have a significant impact on electronic conductivity, by doping the polymer backbone and increasing the charge carrier density; this doping process is reversible under certain conditions, including heating above the glass transition temperature, or under vacuum exposure.^{41,42} LiTFSI is commonly considered to not be a dopant molecule in polythiophenes, but some forms of LiTFSI-assisted doping process have been observed to occur.⁴³

Exemplary Nyquist plots with inserted equivalent fitting are shown in Fig. 8B–D, the assessment and generation of which are discussed here. For P3APPT with $r = 0.05$, the Nyquist plots consist of two semicircles, which is a signature of mixed conducting behavior of electrons and ions. The diameter in the first semicircle on the left corresponds to the combined contribution of ionic resistance (R_{ion}) and electronic resistance (R_{e}). The total diameter of both semicircles towards the right corresponds to

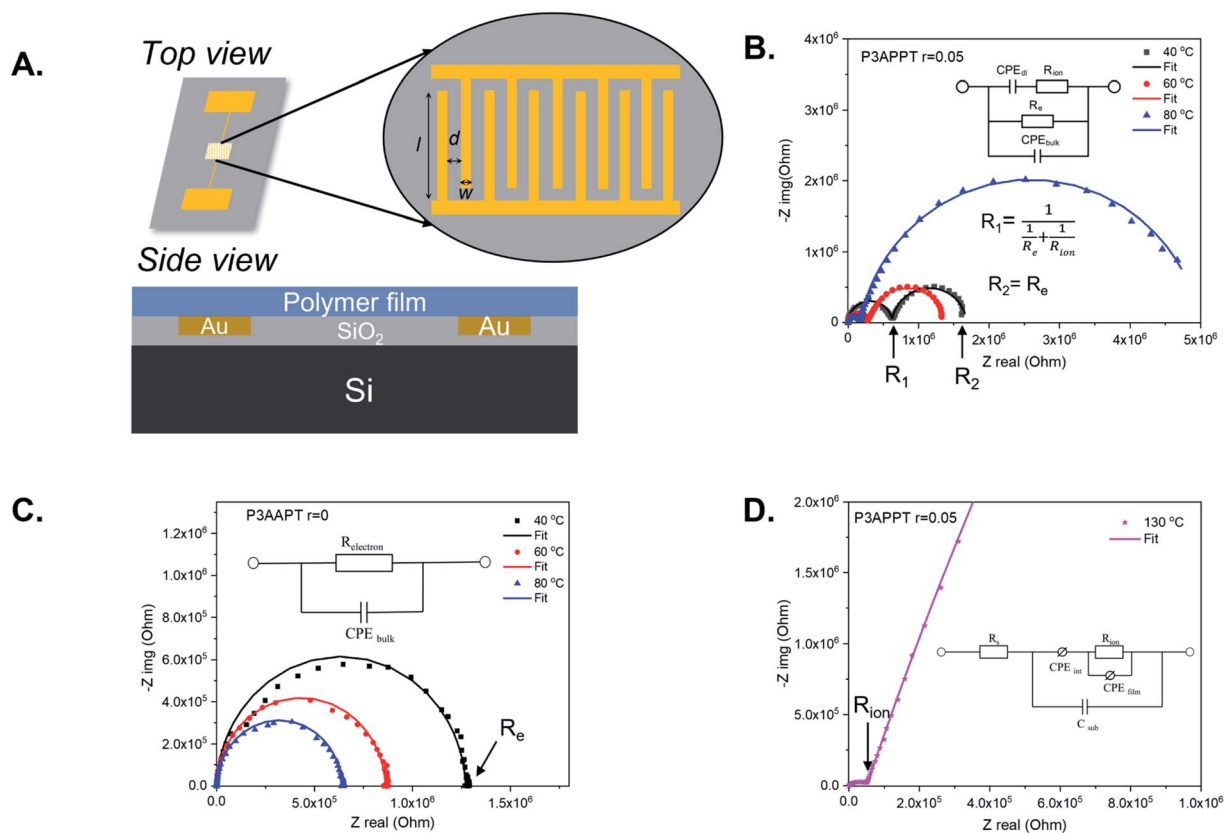


Fig. 8 (A) Schematic top and side views of the interdigitated electrode arrays (IDEs). Exemplary Nyquist plots with insets showing equivalent circuits used for fitting the data and extracting relevant conductivity data for P3APPT at $r = 0.05$ (B), P3AAPT at $r = 0$ (C), and P3APPT at $r = 0.05$ (D). The solid markers corresponds to the experimental data and the curves correspond to the fit using the equivalent circuit shown in the inset.

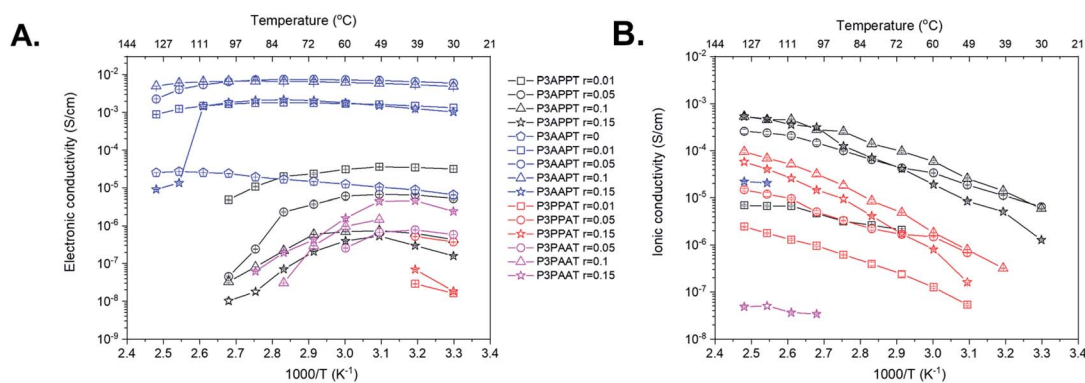


Fig. 9 Summarized extracted EIS data, showing electronic conductivity (A) and ionic conductivity (B) for all polymers and all LiTFSI concentrations (r). Note that the relative error is small, and the resultant error bars overlap the data point markers.

the R_e . To quantify the mixed conductivities of ions and electrons, EIS data were fit to an equivalent circuit with two parallel resistors, R_e and R_{ion} , indicating a simultaneous conduction of ions and electrons. For P3AAPT without LiTFSI dopants (neat P3AAPT), the Nyquist plots consist of one semicircle. The diameter of the semicircle corresponds to the R_e . P3APPT with LiTFSI at temperatures >100 °C was fit to an equivalent circuit with only one resistor R_{ion} , due to the negligible electronic conduction at high temperature.⁴⁴

P3AAPT shows high electronic conductivity, dominating its ionic conductivity for the majority of temperatures and LiTFSI concentrations. The electronic conductivity is also maintained across the full range of tested temperatures, likely due to the relatively high backbone melting temperature. It's notable that there is a nearly 2 order of magnitude increase in electronic conductivity upon introduction of LiTFSI at the relatively small loading $r = 0.01$. The high electronic conductivities of P3AAPT were confirmed with DC measurements. As shown in Fig. S24,†

the electronic conductivities of P3AAPT extracted from EIS and DC measurements are comparable. The maximum electronic conductivity of P3AAPT at $r = 0.1$ was calculated to be $6.72 \times 10^{-3} \text{ S cm}^{-1}$ from EIS and $6.4 \times 10^{-3} \text{ S cm}^{-1}$ from DC, indicating that the measured conductivity arises from electronic transport. Similar, albeit smaller, enhancements in electronic conductivity with LiTFSI introduction are seen in the other polymer systems, likely for similar reasons. For P3APPT and P3PPAT, the increases in electronic conductivity with LiTFSI saturate at higher loading, eventually reversing the trend and causing a reduction in electronic conductivity with increasing LiTFSI.

The increased electronic conductivity of P3AAPT upon the addition of LiTFSI does not seem to be connected to a crystalline morphology change but could be due to an increased ordering in the amorphous domain, though the changes in the UV-vis are relatively small. More likely is the presence of electronic doping from the introduction of LiTFSI. This increased electronic doping results in an increase in charge carrier concentration and can also result in an improved mobility.⁴⁵ Both of these increases can factor into an increase in the electronic conductivity. Similar electronic conductivity performance has also been seen in P3HT homopolymer and P3HT:PEO block copolymers, with several orders of magnitude increases in conductivity with LiTFSI addition.⁴⁴ D. Mombrú *et al.* demonstrates that LiTFSI salts can effectively work as electron acceptors when located near the thiophene rings in P3HT through the formation of π -Li chemical bonds with an anchoring mechanism, permitting hole doping of the thiophene ring.⁴⁶

It's notable that though there is only a limited window of observable ionic conductivity of P3AAPT due to the dominant electronic transport, at a high salt loading and temperature it appears to be outperforming the P3PAAT and is roughly comparable to the P3PPAT, though it is significantly worse than the P3APPT. Overall, though a far stronger electronic conductor, P3AAPT does show workable ionic and electronic conductivities.

As temperature is increased for all P3APPT samples the electronic conductivity decreases, dropping off to unmeasurable levels above 100 °C, likely due either to the onset of backbone melting or to thermal O₂ dedoping.⁴⁷ Similar reductions are also seen in P3PAAT; given the relative lack of backbone crystallinity in P3PAAT, this is likely due to thermal O₂ dedoping. There is an initial increase in electronic conductivity from $r = 0$ to 0.01, after which the further addition of LiTFSI results in an electronic conductivity decrease. It seems reasonable that the reduction in the crystallinity (as observed by the decline in the diffraction intensity and the DSC thermal transitions) correspond well to the decrease in electronic conductivity with increasing LiTFSI concentration.^{48,49} The ionic conductivity of P3APPT presents an interesting trend. As LiTFSI increases from $r = 0.01$ to 0.05, the ionic conductivity increases, as expected; however, above $r = 0.05$, the ionic conductivity remains largely unchanging. We postulate that this is due to both incomplete dissociation of the additional LiTFSI, and the counterbalancing effects of increasing ion concentration and increased glass transition temperature through transient crosslinking of the

side chain, a phenomenon commonly observed in PEO-side chain based ion conductors.^{50–52} The best balance between ionic and electronic conductivities for P3APPT occurs at $r = 0.05$. It presents sufficient salt concentration to enable high ionic conductivity, but not so much to cause extensive disruption of polymer crystallinity and thus decrease electronic conductivity.

The deeply unfavorable oxygen position and low oxygen content in P3PAAT's side chain results in extremely poor performance as an ionic conductor and an only intermediate performance as an electronic conductor. Much like P3APPT, the electronic conductivity consistently decreases with increasing temperature. As r increases electronic conductivity improves, though the variation is relatively small. The ionic conductivity of P3PAAT is poor across all temperatures, which could be due to a reduced LiTFSI solubility, leading to a low effective ion concentration, or due to poor solvation site connectivity.

Due to its limited crystallinity, high oxygen content, and oxygen atom proximity to the backbone, P3PPAT represents the worst electronic conductor of the set with only minimal electronic conductivity, and then only at temperatures close to ambient. The ionic conductivity of P3PPAT is of moderate performance, and with increasing LiTFSI follows a typical pattern of initial increase due to increased ion concentration into an eventual reduction, possibly due to transient crosslinking at high LiTFSI concentrations. The maximum ionic and electronic conductivities observed for all polymers is shown in Table 2.

Comparing the observed ionic conductivities, we see that the measured and simulated amorphous system trends are aligned, though the magnitude of experimental differences significantly exceed the simulations. Comparing P3MEEMT and P3APPT, the simulation results showed the ionic conductivity of P3MEEMT should be approximately twice that of P3APPT, but the measured values are quite comparable (P3MEEMT = $3.8 \times 10^{-4} \text{ S cm}^{-1}$ at 130 °C and $r = 0.05$, P3APPT = $5.4 \times 10^{-4} \text{ S cm}^{-1}$ at 120 °C and $r = 0.10$).¹⁵ Similarly, P3PPAT was found to outperform P3AAPT in the simulation, but are comparable in the experiments. While P3PAAT was simulated to be the worst performer by a small margin, the measured ionic conductivity was several orders of magnitude worse than P3AAPT. We attribute this distinction to the effects of LiTFSI solubility. It's possible that the influence of incomplete dissociation and the formation of ion pairs and ion aggregates which would not be captured by our E_d simulations, could limit the performance of P3PAAT. Overall though, the simulations were able to capture the trends in performance for the synthesized polymers and provide insights into the nature of performance differences across polymer backbones.

It is apparent that increasing the distance along the side chain before a coordinating atom is introduced results in an improvement of the electronic conductivity, as the two highest performing electronic conductors are P3AAPT and P3APPT. It is also observed that the introduction of additional coordinating atoms also results in a reduction in electronic conductivity, as both P3APPT and P3PPAT show reduced performance compared against P3AAPT and P3PAAT, respectively. The

Table 2 Maximum observed ionic and electronic conductivities for all polymer samples. Values are selected from a specific temperature and LiTFSI concentration, which are listed in each cell

	P3AAPT	P3APPT	P3PAAT	P3PPAT
Max ionic conductivity (S cm ⁻¹)	$2.22 \times 10^{-5} \pm 6 \times 10^{-7}$ (at 130 °C, $r = 0.15$)	$5.4 \times 10^{-4} \pm 2 \times 10^{-5}$ (at 130 °C, $r = 0.10$)	$5.1 \times 10^{-8} \pm 5 \times 10^{-9}$ (at 120 °C, $r = 0.15$)	$9.6 \times 10^{-5} \pm 6 \times 10^{-6}$ (at 130 °C, $r = 0.10$)
Max electronic conductivity (S cm ⁻¹)	$7.47 \times 10^{-3} \pm 3 \times 10^{-5}$ (at 70 °C, $r = 0.05$)	$3.60 \times 10^{-5} \pm 2 \times 10^{-7}$ (at 50 °C, $r = 0.01$)	$4.63 \times 10^{-6} \pm 2 \times 10^{-8}$ (at 40 °C, $r = 0.15$)	$5.23 \times 10^{-7} \pm 4 \times 10^{-9}$ (at 40 °C, $r = 0.05$)

relative strength of this effect is less than that of increasing distance, as the electronic conductivity of P3APPT outperforms P3PAAT. The ionic conductivity shows the same two dependences, however, the relative strength is reversed, as two coordinating atoms is more indicative of high ionic conductivity than coordinating atom distance from the polymer backbone. By introducing an additional oxygen atom further along the side chain than in P3PAAT, as in the polymer P3PPAT, results in a 3 order of magnitude improvement in ionic conductivity, and a polymer that outperforms even P3AAPT in spite of the limited coordinating atom-backbone distance. P3APPT, which combines distance and two coordinating atoms, results in the best balance of performance. Maintaining a high number of coordinating groups per repeat unit and high solvation site connectivity, while also increasing the distance between coordinating groups and the backbone provides a pathway to high ionic and electronic conductivity within the same polymer backbone.

4. Conclusions

A series of oEG-substituted polymers with side chains containing varying oxygen contents and positions were investigated both computationally and experimentally, seeking to understand the interplay between the side chain chemical structure and the resultant morphology, ionic conductivity, and electronic conductivity. Molecular dynamics simulations were used to understand how changing the coordinating group position and density would change ionic conductivity in both crystalline and amorphous systems. For the crystalline system, reducing the number of oxygen atoms in the polymer side chain while moving the remaining oxygen atoms as far away from the polymer backbone as possible maximized ionic conductivity, while the amorphous system required more oxygen atoms at a greater distance from the polymer backbone for high ionic conductivity. A selection of these polymers were then synthesized and characterized to understand their molecular structure and the influence of LiTFSI on their structure and conductivity. The collected ionic conductivity data follow a similar trend as seen in the MD simulations for the amorphous systems; pushing the oxygen atom density away from the polymer backbone improves the ionic conductivity. An additional benefit that was observed was that this increased oxygen atom distance also resulted in improved backbone crystallinity and results in an improvement of the electronic conductivity. P3APPT, with the additional space between backbone and oxygen atoms in the side chain, results in ionic conductivities

comparable to P3MEEMT while also having better electronic conductivity. This provides insight into a strategy for designing higher performance MIECs – increase the coordinating group distance from the backbone and reduce the number of coordinating groups while maintaining solvation site interconnectivity. From this, it is possible to adjust the balance of ionic conductivity and electronic conductivity by adjusting the substitution pattern of the side chain, enabling tuning of the polymer for different applications. One unanswered question is whether these observed trends will be maintained when the polymers are swelled with water during injection of hydrated salts, as is the case with standard OECT operation. Future work investigating such considerations will be important to understanding the translation of dry-state properties to operation under solvent swelled conditions.

Author contributions

J. W. O. was responsible for conceptualization, formal analysis, investigation, visualization, writing – original draft, and writing – review & editing. Z. W. was responsible for conceptualization, formal analysis, investigation, reviewing and editing. Y. S. was responsible for conceptualization, formal analysis, investigation, and software. C. N. was responsible for software and conceptualization. L. Q. F. was responsible for formal analysis and investigation. R. L. was responsible for investigation. B. X. D. was responsible for conceptualization. L. J. R. was responsible for formal analysis and supervision. F. E. was responsible for supervision. P. N. was responsible for supervision. S. P. was responsible for supervision. C. K. L. was responsible for supervision and writing – review & editing.

Conflicts of interest

There are no conflicts to declare.

Acknowledgements

This work was funded in part through NSF DMREF award number 1922259. Part of this work was conducted at the Washington Clean Energy Testbeds, a facility supported by the state of Washington through the University of Washington Clean Energy Institute. Part of this work was performed at the Soft Matter Characterization Facility of the University of Chicago. This work made use of the Pritzker Nanofabrication Facility of the Pritzker School of Molecular Engineering at the University of Chicago, which receives support from Soft and

Hybrid Nanotechnology Experimental (SHyNE) Resource (NSF ECCS-1542205), anode of the National Science Foundation's National Nanotechnology Coordinated Infrastructure. This work made use of the shared facilities at the University of Chicago Materials Research Science and Engineering Center, supported by National Science Foundation under award number DMR-2011854. This research used resources of the National Synchrotron Light Source II, a U.S. Department of Energy (DOE) Office of Science User Facility operated for the DOE Office of Science by Brookhaven National Laboratory under Contract No. DE-SC0012704.

References

- 1 A. Giovannitti, D.-T. Sbircea, S. Inal, C. B. Nielsen, E. Bandiello, D. A. Hanifi, M. Sessolo, G. G. Malliaras, I. McCulloch and J. Rivnay, *Proc. Natl. Acad. Sci. U. S. A.*, 2016, **113**, 12017–12022.
- 2 S. Wustoni, T. C. Hidalgo, A. Hama, D. Ohayon, A. Savva, N. Wei, N. Wehbe and S. Inal, *Adv. Mater. Technol.*, 2020, **5**, 1900943.
- 3 A. Savva, S. Wustoni and S. Inal, *J. Mater. Chem. C*, 2018, **6**, 12023–12030.
- 4 A. M. Pappa, D. Ohayon, A. Giovannitti, I. P. Maria, A. Savva, I. Uguz, J. Rivnay, I. McCulloch, R. M. Owens and S. Inal, *Sci. Adv.*, 2018, **4**, eaat0911.
- 5 H. Zhao, B. Zhu, J. Sekine, S.-C. Luo and H. Yu, *ACS Appl. Mater. Interfaces*, 2012, **4**, 680–686.
- 6 B. Kim, J. Un Hwang and E. Kim, *Energy Environ. Sci.*, 2020, **13**, 859–867.
- 7 P. Han, S.-H. Chung and A. Manthiram, *Energy Storage Mater.*, 2019, **17**, 317–324.
- 8 S. T. Keene, C. Lubrano, S. Kazemzadeh, A. Melianas, Y. Tuchman, G. Polino, P. Scognamiglio, L. Cinà, A. Salleo, Y. van de Burgt and F. Santoro, *Nat. Mater.*, 2020, 1–5.
- 9 J. Stejskal, O. E. Bogomolova, N. V. Blinova, M. Trchová, I. Šeděnková, J. Prokeš and I. Sapurina, *Polym. Int.*, 2009, **58**, 872–879.
- 10 C. H. W. Cheng, F. Lin and M. C. Lonergan, *J. Phys. Chem. B*, 2005, **109**, 10168–10178.
- 11 S. Inal, J. Rivnay, P. Leleux, M. Ferro, M. Ramuz, J. C. Brendel, M. M. Schmidt, M. Thelakkat and G. G. Malliaras, *Adv. Mater.*, 2014, **26**, 7450–7455.
- 12 A. Pipertzis, M. Mühlinghaus, M. Mezger, U. Scherf and G. Floudas, *Macromolecules*, 2018, **51**, 6400–6450.
- 13 S. Inal, G. G. Malliaras and J. Rivnay, *Nat. Commun.*, 2017, **8**, 1767.
- 14 A. Giovannitti, C. B. Nielsen, D.-T. Sbircea, S. Inal, M. Donahue, M. R. Niazi, D. A. Hanifi, A. Amassian, G. G. Malliaras, J. Rivnay and I. McCulloch, *Nat. Commun.*, 2016, **7**, 13066.
- 15 B. X. Dong, C. Nowak, J. W. Onorato, J. Strzalka, F. A. Escobedo, C. K. Luscombe, P. F. Nealey and S. N. Patel, *Chem. Mater.*, 2019, **31**, 1418–1429.
- 16 A. Giovannitti, I. P. Maria, D. Hanifi, M. J. Donahue, D. Bryant, K. J. Barth, B. E. Makdah, A. Savva, D. Moia, M. Zetek, P. R. F. Barnes, O. G. Reid, S. Inal, G. Rumbles, G. G. Malliaras, J. Nelson, J. Rivnay and I. McCulloch, *Chem. Mater.*, 2018, **30**, 2945–2953.
- 17 B. Meng, H. Song, X. Chen, Z. Xie, J. Liu and L. Wang, *Macromolecules*, 2015, **48**, 4357–4363.
- 18 B. Meng, J. Liu and L. Wang, *Polym. Chem.*, 2020, **11**, 1261–1270.
- 19 P. Schmode, A. Savva, R. Kahl, D. Ohayon, F. Meichsner, O. Dolynchuk, T. Thurn-Albrecht, S. Inal and M. Thelakkat, *ACS Appl. Mater. Interfaces*, 2020, **12**, 13029–13039.
- 20 D. Ohayon, A. Savva, W. Du, B. D. Paulsen, I. Uguz, R. S. Ashraf, J. Rivnay, I. McCulloch and S. Inal, *ACS Appl. Mater. Interfaces*, 2021, **13**, 4253–4266.
- 21 D. Nečas and P. Klapetek, *Cent. Eur. J. Phys.*, 2012, **10**, 181–188.
- 22 F. Zhang, J. Ilavsky, G. G. Long, J. P. G. Quintana, A. J. Allen and P. R. Jemian, *Metall. Mater. Trans. A*, 2010, **41**, 1151–1158.
- 23 J. Ilavsky, *J. Appl. Crystallogr.*, 2012, **45**, 324–328.
- 24 D. Sharon, P. Bennington, C. Liu, Y. Kambe, B. X. Dong, V. F. Burnett, M. Dolejsi, G. Grocke, S. N. Patel and P. F. Nealey, *J. Electrochem. Soc.*, 2018, **165**, H1028.
- 25 B. X. Dong, Z. Liu, M. Misra, J. Strzalka, J. Niklas, O. G. Poluektov, F. A. Escobedo, C. K. Ober, P. F. Nealey and S. N. Patel, *ACS Nano*, 2019, **13**, 7665–7675.
- 26 G. M. Torrie and J. P. Valleau, *J. Comput. Phys.*, 1977, **23**, 187–199.
- 27 A. de Izarra, C. Choi, Y. H. Jang and Y. Lansac, *J. Phys. Chem. B*, 2021, **125**, 1916–1923.
- 28 J.-F. Chang, B. Sun, D. W. Breiby, M. M. Nielsen, T. I. Sölling, M. Giles, I. McCulloch and H. Sirringhaus, *Chem. Mater.*, 2004, **16**, 4772–4776.
- 29 J. Y. Na, M. Kim and Y. D. Park, *J. Phys. Chem. C*, 2017, **121**, 13930–13937.
- 30 L. Farouil, F. Alary, E. Bedel-Pereira and J.-L. Heully, *J. Phys. Chem. A*, 2018, **122**, 6532–6545.
- 31 N. J. Hestand and F. C. Spano, *Chem. Rev.*, 2018, **118**, 7069–7163.
- 32 K. Rahimi, I. Botiz, J. O. Agumba, S. Motamen, N. Stingelin and G. Reiter, *RSC Adv.*, 2014, **4**, 11121–11123.
- 33 C. R. Snyder, R. C. Nieuwendaal, D. M. DeLongchamp, C. K. Luscombe, P. Sista and S. D. Boyd, *Macromolecules*, 2014, **47**, 3942–3950.
- 34 M. J. Marczewski, B. Stanje, I. Hanzu, M. Wilkening and P. Johansson, *Phys. Chem. Chem. Phys.*, 2014, **16**, 12341–12349.
- 35 Z. Qian, L. Galuska, W. W. McNutt, M. U. Ocheje, Y. He, Z. Cao, S. Zhang, J. Xu, K. Hong, R. B. Goodman, S. Rondeau-Gagné, J. Mei and X. Gu, *J. Polym. Sci., Part B: Polym. Phys.*, 2019, **57**, 1635–1644.
- 36 S. E. Root, M. A. Alkhadra, D. Rodriguez, A. D. Printz and D. J. Lipomi, *Chem. Mater.*, 2017, **29**, 2646–2654.
- 37 L. Q. Flagg, C. G. Bischak, J. W. Onorato, R. B. Rashid, C. K. Luscombe and D. S. Ginger, *J. Am. Chem. Soc.*, 2019, **141**, 4345–4354.
- 38 R. Giridharagopal, L. Q. Flagg, J. S. Harrison, M. E. Ziffer, J. Onorato, C. K. Luscombe and D. S. Ginger, *Nat. Mater.*, 2017, **16**, 737–742.

- 39 A. Savva, C. Cendra, A. Giugni, B. Torre, J. Surgailis, D. Ohayon, A. Giovannitti, I. McCulloch, E. Di Fabrizio, A. Salleo, J. Rivnay and S. Inal, *Chem. Mater.*, 2019, **31**, 927–937.
- 40 W. Liu, L. Müller, S. Ma, S. Barlow, S. R. Marder, W. Kowalsky, A. Köhn and R. Lovrincic, *J. Phys. Chem. C*, 2018, **122**, 27983–27990.
- 41 H.-H. Liao, C.-M. Yang, C.-C. Liu, S.-F. Horng, H.-F. Meng and J.-T. Shy, *J. Appl. Phys.*, 2008, **103**, 104506.
- 42 M. L. Chabinye, R. A. Street and J. E. Northrup, *Appl. Phys. Lett.*, 2007, **90**, 123508.
- 43 A. Abate, T. Leijtens, S. Pathak, J. Teuscher, R. Avolio, M. E. Errico, J. Kirkpatrick, J. M. Ball, P. Docampo, I. McPherson and H. J. Snaith, *Phys. Chem. Chem. Phys.*, 2013, **15**, 2572–2579.
- 44 S. N. Patel, A. E. Javier, G. M. Stone, S. A. Mullin and N. P. Balsara, *ACS Nano*, 2012, **6**, 1589–1600.
- 45 Y. Harima, X. Jiang, Y. Kunugi, K. Yamashita, A. Naka, K. K. Lee and M. Ishikawa, *J. Mater. Chem.*, 2003, **13**, 1298–1305.
- 46 D. Mombrú, M. Romero, R. Faccio and Á. W. Mombrú, *J. Phys. Chem. C*, 2020, **124**(13), 7061–7070.
- 47 M. S. A. Abdou, F. P. Orfino, Y. Son and S. Holdcroft, *J. Am. Chem. Soc.*, 1997, **119**, 4518–4524.
- 48 S. A. Mollinger, B. A. Krajina, R. Noriega, A. Salleo and A. J. Spakowitz, *ACS Macro Lett.*, 2015, **4**, 708–712.
- 49 K. Gu and Y.-L. Loo, *J. Polym. Sci., Part B: Polym. Phys.*, 2019, **57**, 1559–1571.
- 50 M. Digar, S. L. Hung, H. L. Wang, T. C. Wen and A. Gopalan, *Polymer*, 2002, **43**, 681–691.
- 51 S. Seki, Md. A. B. H. Susan, T. Kaneko, H. Tokuda, A. Noda and M. Watanabe, *J. Phys. Chem. B*, 2005, **109**, 3886–3892.
- 52 A. Nishimoto, K. Agehara, N. Furuya, T. Watanabe and M. Watanabe, *Macromolecules*, 1999, **32**, 1541–1548.